J Supercond Nov Magn (2016) 29:1923–1930
DOI 10.1007/s10948-016-3490-6

ORIGINAL PAPER

Conductivity and Dielectric Properties of Nearly Monodisperse $NiFe_2O_4$ Nanoparticles

U. Kurtan[1] · H. Erdemi[2] · D. Dursun[1] · A. Baykal[1]

Received: 10 March 2016 / Accepted: 16 March 2016 / Published online: 30 March 2016

Abstract Oleylamine (OAm) functionalized $NiFe_2O_4$ nanoparticles were synthesized by reflux method. Oleylamine as a multufunctional ligand provides the essential basic condition for the formation of $NiFe_2O_4$ nanoparticles, and it has also surfactant and reducing agent roles. The product was characterized by X-ray diffraction analysis (XRD), transmission electron microscopy (TEM), vibrating sample magnetometry, and thermal gravimetric analyzer (TG). The detailed electrical conductivity and dielectric property of measurements have been performed by dielectric impedance analyzer. The conductivity results show that ac conductivity (σ_{ac}) is temperature dependent particularly at low frequencies whereas dc conductivity (σ_{dc}) exhibits only temperature dependency. The highest dc conductivity is 4.37×10^{-12} S.cm^{-1} at 120 °C. The dielectric constant (ε'), dielectric loss (ε''), and dielectric loss tangent (tan δ) show different behaviors with frequency and temperature. The variation of dielectric properties with temperature is mainly due to temperature-assisted electron exchange between Ni^{2+} and Fe^{3+} ions.

Keywords $NiFe_2O_4$ · Dielectric spectroscopy · Electrical properties · Reflux method · Oleylamine

✉ A. Baykal
hbaykal@fatih.edu.tr

[1] Department of Chemistry, Fatih University, 34500 B.Çekmece, İstanbul, Turkey

[2] Department of Polymer Engineering, Yalova University, 77100 Yalova, Turkey

1 Introduction

Monodisperse spinel ferrites with a narrow size distribution have been intensively investigated because of their good electrical characteristics in recent years [1, 2]. Since the dielectric properties of these kinds of substances with different temperatures, compositions, and frequencies, it is gaining so much interest to obtain a high-quality spinel type of material. In addition, dielectric behavior allows having sufficient information about the mechanism of dielectric polarization in spinel-type ferrites [3–5].

$NiFe_2O_4$, which is one of the mostly studied ferrites, has been proposed by the researchers in many fields of electronic devices, magnetic resonance imaging, hyperthermia, magnetoelectric (ME) applications, data storage information, and Li-ion batteries as anode materials and among others [6–9].

Up to date, a variety of methods to prepare $NiFe_2O_4$ NPs have been already explored in the literature such as thermal treatment, microwave synthesis, combustion method, and ethylene glycol route [10–14]. However, the problems with these common routes are that the synthesized nanoparticles have generally a tendency of agglomeration with uncontrollable shape and size, which mostly make some applications impossible [14]. Among these synthesis methods, the thermal decomposition of inorganic precursors in a high-boiling-point organic solvent like benzyl ether is one of the most effective ways to synthesize monodisperse magnetic nanoparticle (MNPs). Also, OAm was used in the production of nanomaterials containing at least one magnetic element in the literature [15, 16], because its high boiling point (∼350 °C) allows the chance to study with strong heating reaction conditions and it can also become a surfactant and even a mild reducing agent. From this

viewpoint, it can be considered as a "multifunctional role" (reducing agent, surfactant, and stabilizing agent) in the synthesis of monodisperse $NiFe_2O_4$ NPs. To the best of our knowledge, this is the first study in which conductivity and dielectric properties of OAm functionalized $NiFe_2O_4$ NPs have been investigated.

2 Experimental

2.1 Chemicals and Instrumentation

$Ni(acac)_2$, $Fe(acac)_3$, oleylamine (OAm), and benzyl ether were acquired from Merck and used as received without further purification.

The samples were characterized by X-ray diffraction (XRD) to investigate the crystalline structure and average particle size. X-ray diffraction patterns were obtained with a Rigaku D/Max—IIIC X-ray diffractometer using Cu-Kα radiation over Bragg angles from 20° to 70° with the scanning speed of 4°/min.

Fourier transform infrared (FT-IR) spectra were recorded in transmission mode with a Perkin Elmer BX FT-IR infrared spectrometer in the range 4000–400 cm^{-1} to investigate the nature of the chemical bonds formed.

Transmission electron microscopy (TEM) analysis was performed using FEI Tecnai G2 Sphera microscope. A drop of diluted sample in alcohol was dripped on a TEM grid and dried prior to insertion to the TEM column.

The electrical conductivity of the $NiFe_2O_4$ NPs was studied in the temperature range of 20–120 C with a heating rate of 10 °C/s. The sample was used in the form of circular pellets of 13 mm diameter and 3 mm thickness. The pellets (both nanocomposite and pristine) were sandwiched between gold electrodes and the conductivities were measured using Novocontrol dielectric impedance analyzer in the frequency range of 1 Hz–3 MHz, respectively. The temperature (between 100 and 250 °C) was controlled with a Novocool Cryosystem.

2.2 Synthesis of $NiFe_2O_4$ NPs

The synthesis of the product was reported in our previous study [17]. Shortly, the salts of $Ni(acac)_2$ and $Fe(acac)_3$ was used as 1:2 ratio (1:2 mmol) and dissolved in 15 ml benzyl ether and 15 ml of oleylamine mixture by stirring to get a homogeneous solution. After drying the above solution at 110 °C for 1 h under N_2 atmosphere in the heating mantle, temperature was rapidly increased to 300 °C and was hold at that temperature for 1 h (Fig. 1). Then final solution was cooled down to room temperature; solid product was extracted ethylacetate-ethanol mixture by centrifugation and was washed ethanol again and centrifuged once more. The final sample was further hold at 150 °C until it completely becomes a dry powder (Fig. 1).

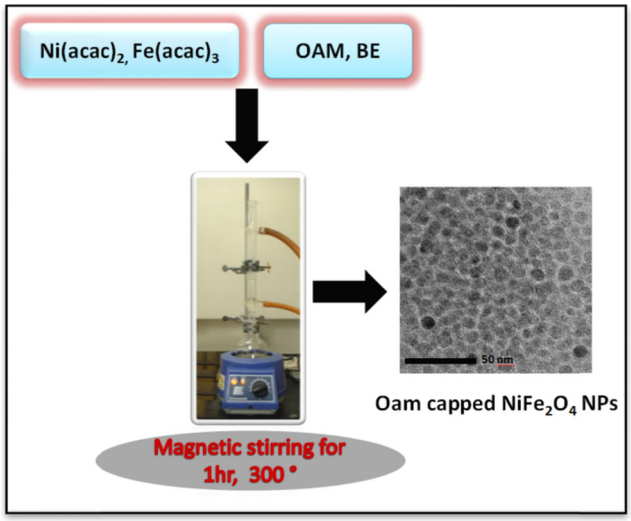

Fig. 1 Schematic representation of synthesis of OAm functionalized $NiFe_2O_4$ NPs

3 Results and Discussion

3.1 Characterizations

X-ray diffraction powder pattern of the OAm functionalized $NiFe_2O_4$ NPs sample is presented in Fig. 2a. All the diffraction peaks given in Fig. 2a matched with the standard ICDD card (10-0325) of $NiFe_2O_4$. Due to the broadening diffraction peaks given in Fig. 2a, small-sized nanoparticles were formed. The crystallite size calculated by Debby Scherer formula was 6.1 nm [18]. In order to confirm the presence of OAm on the surface of $NiFe_2O_4$ NPs, FT-IR analysis was conducted. The FT-IR spectrum of OAm functionalized $NiFe_2O_4$ NPs is given in Fig. 2b in which the bands at 2933 and 2870 cm^{-1} were ascribed to the asymmetric and symmetric stretching vibration of the CH_2 groups, respectively, and the bands at 1234–1532 cm^{-1} were assigned to the long hydrocarbon chain of oleylamine. The bands 1060 and 980 cm^{-1} are attributed to the =C–H out-of-plane and in-plane bending, respectively. The peak at 758 cm^{-1} is corresponded to the C–C and NH_2 bending mode [19]. Also, it should be noticed that the spectrum has also low-frequency bands of the spinel structured nickel ferrite, that is, the band at 670 and 506 cm^{-1} refer to metal-oxygen stretching vibrations [14, 20, 21]. Thus, the FT-IR spectrum demonstrates that the nanoparticles are capped by OAm successfully, which can ensure repulsive forces to equalize the attractive forces such as dipole–dipole interaction or van der Waals forces between the nanoparticles [22].

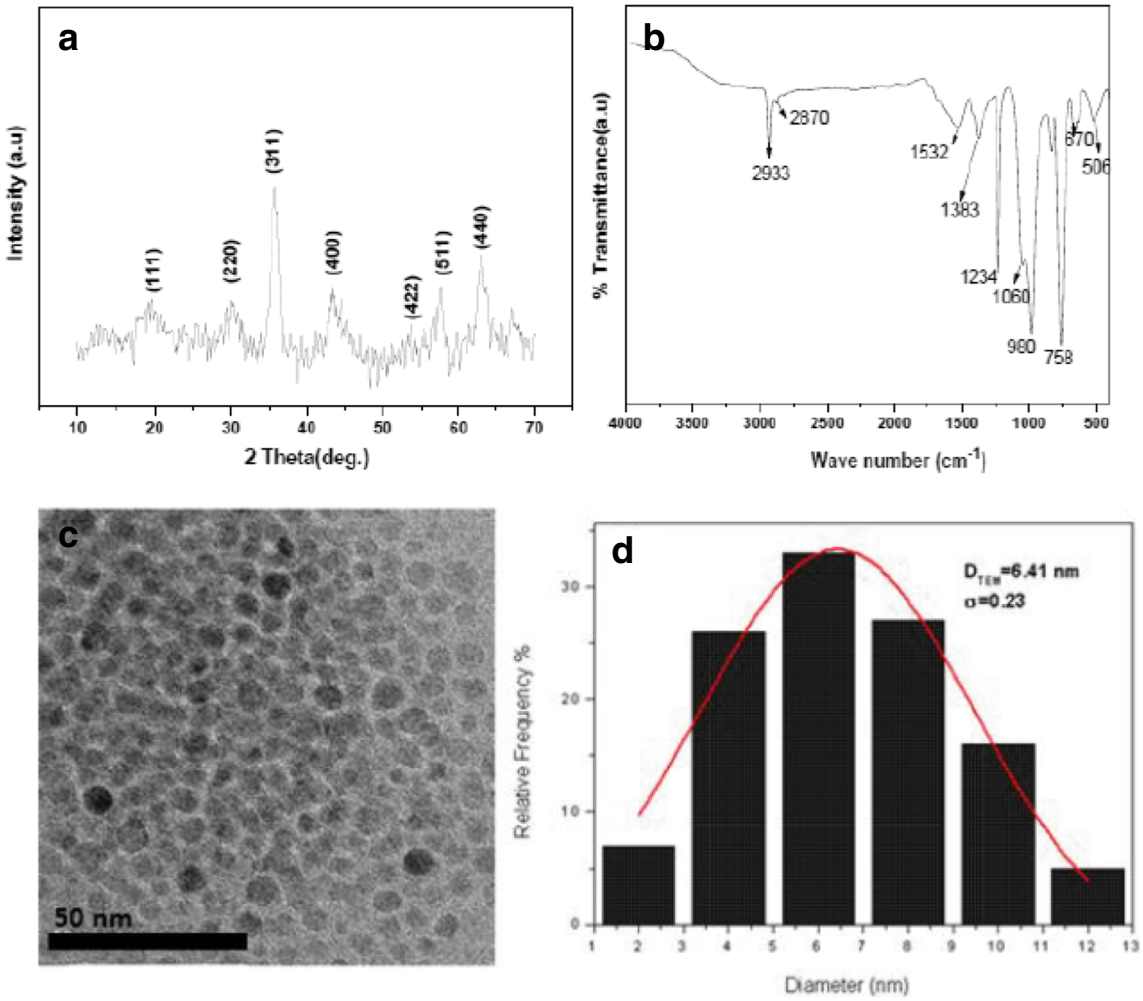

Fig. 2 **a** Representative X-ray diffraction pattern, **b** FT-IR spectra, **c** TEM image, and **d** the corresponding particle size distributions

The transmission electron microscopy (TEM) images of OAm functionalized $NiFe_2O_4$ NPs are shown in Fig. 2c. It can be observed in these figures that a low aggregation and high narrow size have been obtained. Also, it can be seen from the corresponding size distribution histogram in Fig. 2d that the size distribution of the $NiFe_2O_4$ NPs is very narrow and nearly monodisperse structure. The size of the nanocrystals obtained from the XRD diffraction patterns is in close agreement with the TEM studies which show sizes of 6.4.

3.2 Electrical Properties

3.2.1 ac Conductivity

Figure 3 displays the variations in ac conductivity of OAm functionalized $NiFe_2O_4$ NPs, σ_{ac} (ω), with frequency in the range of 1 Hz–1 MHz at temperatures from 20 to 120 °C. The frequency-dependent ac conductivity is examined by using the following standard equation (1):

$$\sigma'(\omega) = \sigma_{ac}(\omega) = \varepsilon''(\omega)\omega\varepsilon_0 \quad (1)$$

where σ' (ω) is the real part of conductivity, $\omega = 2\pi f$ is the angular frequency of the applied field, ε? is the dielectric loss, and ε_0 (8.852×10^{-14} F cm^{-1}) is permittivity of free space.

The frequency-dependent ac conductivity plots exhibit closely trend at all temperatures in the log–log graph. In the low-frequency regime, linear increase is assigned to the blocking electrode polarizations at low temperatures. The substantial temperature-dependent behavior was observed at low and medium frequencies while it indicates temperature independency at higher frequencies ($>10^3$ Hz). The ac conductivity rises regularly with temperature up to 10^3 Hz, and subsequently, it turns out to be frequency dependent.

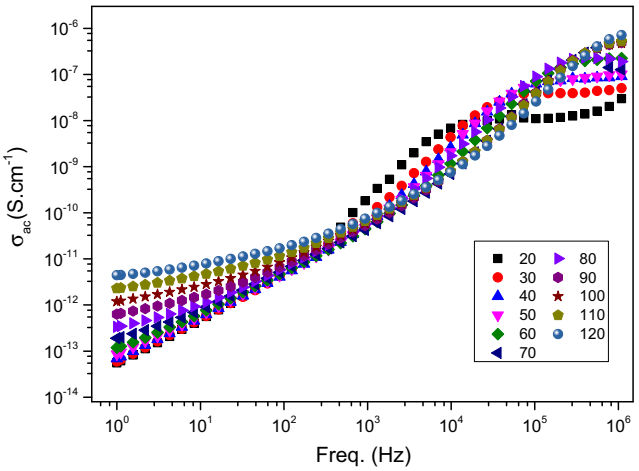

Fig. 3 The variation of ac conductivity of OAm functionalized $NiFe_2O_4$ NPs as a function of frequency and temperature

At low-frequency regions, ac conductivity curves include nearly frequency-independent conductivity plateaus while it shifts and broadens towards higher frequencies with increasing temperature. Displaying a frequency-dependent behavior at moderately higher frequencies and temperature dependency at relatively low frequencies may suggest ionic conductivity [23, 24].

The linear increase in σ_{ac}, which becomes more clearly above a phase transition zone (50–60 °C), develops an almost equivalent slope for all temperatures. With regard to ac conductivity at 100 Hz before and after the transition zone, it improved from 4.07×10^{-12} to 4.36×10^{-12} as temperature increased from 40 to 50 °C, while the conductivity raised from 4.67×10^{-12} to 5.11×10^{-12} as temperature varied from 60 to 70 °C. The ionic conductivity over phase transition region also contributes considerably to conductivity which leads to such an improvement in ac conductivity [24, 25]. The diffusion of charge carriers increases with temperatures because of the effect of the local dynamics and enhancement of connectivity among the sites in nanocomposites. Initially, the oleylamine-coated $NiFe_2O_4$ NPs build up a randomly distributed network at low temperatures whereas a more organized structure is established as the temperature increases. The OAm functionalized $NiFe_2O_4$ NPs begin to exhibit a weak frequency response and more capacitive behavior on hopping conduction which leads to an increase in conductivity. Furthermore, a percolation between $NiFe_2O_4$ NPs may be improved due to the increase in interaction of nanoparticles with the applied temperature. The percolation leads to flow of electrical current through both semiconducting $NiFe_2O_4$ NPs and oleylamine as reported in literature [26–28].

The random distribution of $NiFe_2O_4$ NPs decides the low- and high-frequency responses. The conductivity of the nanocomposite increases persistently with frequency as percolation exists through the nanocomposite which gives rise to improvement of plateaus over a certain temperature. The reorganization of the OAm functionalized $NiFe_2O_4$ NPs takes place in the phase transition region of 50–60 °C. Consequently, the ac conductivity rises steadily with temperature in Arrhenius plot until 50 °C. After whole reorganization of the OAm functionalized $NiFe_2O_4$ NPs in the transition zone (50–60 °C), the conductivity continued to increase with a considerable increase in slope with reciprocal temperature above 60 °C. This variation is essentially due to the influence of the thermal energy applied on OAm functionalized $NiFe_2O_4$ NPs. It was observed that the conductivity of uncoated $NiFe_2O_4$ NPs is higher as compared with OAm functionalized $NiFe_2O_4$ NPs [29]. The decline in conductivity may be due to the reduction of free surface resulting from surface bonding between $NiFe_2O_4$ NPs and OAm [26, 27].

Figure 4 shows the variations in ac conductivity of OAm functionalized $NiFe_2O_4$ NPs with frequency at different temperatures in *log* σ_{ac}–*log F* plot. The ac conductivity grows nearly linearly with an increase in the studied frequency ranges at all temperatures. The electrical conduction, which is frequency dependent, is basically due to the migration of ions in ionic solids; as a consequence, ac conductivity exhibits a direct correlation with angular frequency [30]. In general, the conduction mechanism of ferrites is described by the jumping of electrons between Fe^{2+} and Fe^{3+} at octahedral (B) sites [31]. Thus, ac conductivity improves with increasing frequency of the applied field as hopping frequency of the charge carriers between Fe^{2+} and Fe^{3+} develops. In the literature, it has been shown that a rather small quantity of Fe^{2+} and Ni^{3+} is produced during the synthesis of this kind of nanoparticles and the

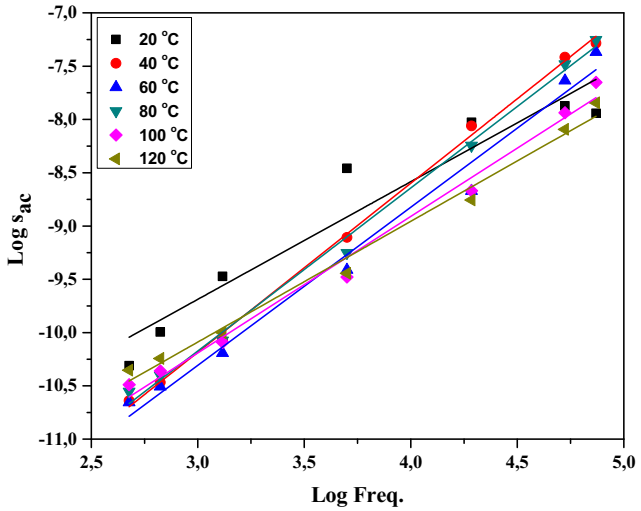

Fig. 4 Log σ_{ac}-log freq. plot of OAm functionalized $NiFe_2O_4$ NPs

electron exchange is supposed to be between the iron and nickel ions as follows [29–32].

$$Ni^{2+} + Fe^{3+} \leftrightarrow Ni^{3+} + Fe^{2+}$$

The increase in conductivity with enhancement in temperature is described by improvement in drift mobility of the charge carriers. At higher temperatures, however, the conduction in ferrites is mainly due to electron transfer from Fe^{3+} to Fe^{2+} [31–33]. In the present study, the gradual increase in ac conductivity with frequency is explained by the influence of the applied frequency that supports movement of charge carriers between the different localized states in addition to releasing the trapped charges from the various trapping centers. The hopping of holes between Ni^{2+} and Ni^{3+} on B site similarly contributes to overall conductivity.

3.2.2 dc Conductivity

The variations in dc conductivity (σ_{dc}) of $NiFe_2O_4$ NPs versus reciprocal temperature is displayed in Fig. 5. The dc conductivities were obtained by extrapolating almost frequency-independent ac conductivity plateau regions to the zero frequency. It is observed that dc conductivity increased in direct proportion to the increase of temperature revealing two separate regions with linear increment and including phase transition region. The temperature-dependent conductivity of two regions follows an Arrhenius law:

$$\log \sigma_{dc} = \log \sigma_0 - E_a / k_B T \quad (2)$$

where σ_{dc} is the dc conductivity at temperature T in K, k_B is the Boltzmann's constant (8.617×10^{-5} eV K^{-1}), E_a is the activation energy, and σ_0 is called the pre-exponential factor. The activation energy, E_a, may be deduced easily from the slope of the log σ_{dc} versus T^{-1} plot. The increase of conductivity with temperature is possibly due to the development in drift mobility of the charge carriers as mentioned before, and this behavior displays the semiconducting characteristics of the samples. The development of two separate regions at low- and high-temperature regions has been reported in literature [26, 28]. Two activation energies were calculated from two separated Arrhenius plots. The low-activation energy for the first region may suggest that the conduction is due to the free charge carriers. The second region exists at higher temperatures, and it requires higher activation energy since the conductivity in this region essentially arises from the hopping of charge carriers. The activation energies for two distinct regions (20–50 °C and 60–120 °C) were calculated as $E_{a1} = 0.0351$ eV and $E_{a2} = 0.299$ eV which is consistent with the similar works as reported [26, 27].

The holes formed due to the oxidation of Ni^{2+} to Ni^{3+} also contributes to conduction. Thus, the change of dc conductivity with temperature depends significantly on the quantity of iron ions at octahedral site as well as the amount of holes.

3.2.3 Dielectric Properties

The change of dielectric constant (ε') and dielectric loss (ε'') with frequency at various temperatures from 20 to 120 °C is depicted in Figs. 6 and 7, respectively.

The dielectric constants (ε') exhibit almost a parabolic decay with frequency up to about 10^3 Hz. The decline is more considerable at the low-frequency region and at high temperatures while it exhibits a slight reduction at low temperatures. At higher frequencies ($>10^3$ Hz), dielectric

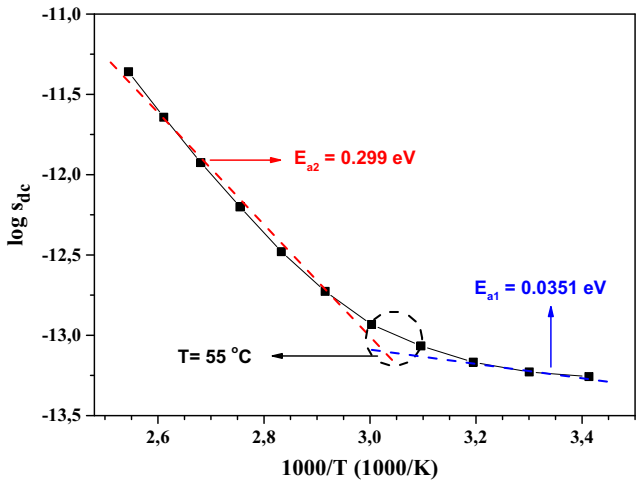

Fig. 5 The variation of dc conductivity of OAm functionalized $NiFe_2O_4$ NPs with reciprocal temperature

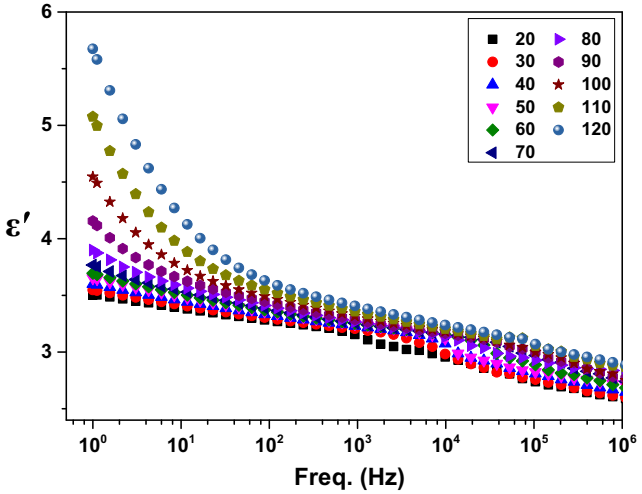

Fig. 6 The dielectric constant of OAm functionalized $NiFe_2O_4$ NPs as a function of frequency at various temperatures

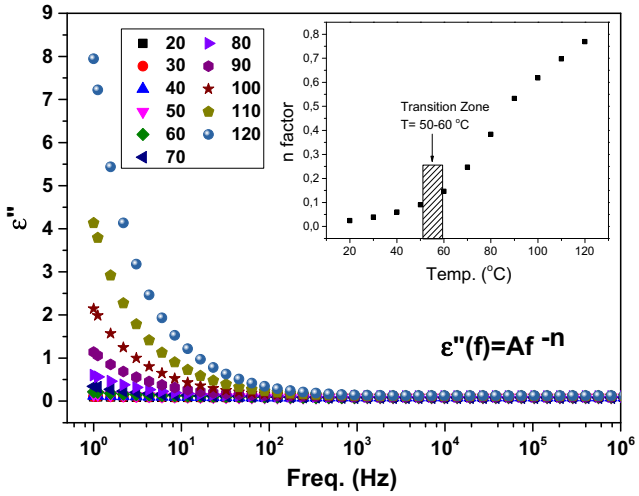

Fig. 7 The dielectric loss of OAm functionalized $NiFe_2O_4$ NPs as a function of frequency at various temperatures with *inset* for frequency exponent "*n*"

constants reach to nearly a constant value which indicates the effect of frequency on the conduction mechanism is insignificant in this interval. The sharp decline in dielectric constant with increase in frequency is principally assigned to the frequency-dependent polarization mechanisms. As the polarizations in ferrites are determined by the exchange of electrons between Fe^{2+} and Fe^{3+} at octahedral sites, the maximum loss occurs when the jumping frequency between Fe^{2+} and Fe^{3+} synchronizes with that of the applied electric field. As a result, the extent of orientational polarization decreases with an increase in frequency as a longer time is required than that for ionic and electronic polarizations [34]. The substantial reduction in dielectric constant as frequency increases may also be due to the material electrode interface polarization existing at lower frequencies [35] .

While concerning the change of dielectric constant with temperature, it grows markedly with temperature particularly at the lower frequency region up to 10^3 Hz. When temperatures increases, a random network formed all over OAm functionalized $NiFe_2O_4$ NPs which provides the stabilization of surface charges and results in a significant increase of dielectric constant. The comparable results of dielectric constant have been already reported for similar studies in literature [36, 37]. The conduction in this kind of NPs is a thermally activated process, and it can be described as the change in mobility of the charge carriers [38].

The dielectric loss constant (ε'') decreases exponentially with frequency, and this decline is more substantial at higher temperatures and at low frequencies. With increasing frequency, it becomes nearly equal at all temperatures. The interaction of Fe^{2+}, Fe^{3+}, Ni^{2+}, and Ni^{3+} ions with adjacent O^{2-} ions results in improvement of dipoles which regulates the electrical properties of ferrites. The dipole interactions develop more at lower frequencies, and it decreases with increasing frequency leading to a significant decline in dielectric loss constant [39]. It is known that the polarization carriers in ferrites is principally a result of the electron exchange between neighboring Fe^{3+} and Fe^{2+} ions at octahedral sites which leads to local displacement of electric charge [40].

The frequency-dependent dielectric properties of such inhomogeneous double-layer structure is basically described by Koops phenomenological theory based on the Maxwell–Wagner interfacial type of polarization [35–37]. This inhomogeneous two layers comprise a rather good conducting sizable ferrite grains. This discontinuous structure is separated by relatively weak conducting grain boundaries. The grain boundaries are known to dominate at lower frequencies while grains determine the dielectric properties of such inhomogeneous structure at higher frequencies [38, 39]. The charge carriers are collected in separated boundaries due to the conductivity differences in grains and grain boundaries leading to interfacial polarization and an improvement in dielectric constants. The influence of interfacial polarization is higher at lower frequencies while electronic and ionic types of mechanisms become more effective with increasing frequency [41, 42]. Grain boundary defects, oxygen vacancies, and local valence deviations also contribute to overall interfacial polarization which results in the increase of dielectric constants at lower frequencies [43].

The frequency dependency of dielectric loss can be investigated by power law, $\varepsilon''(\omega) = A\omega^{-n}$, where A is a pre-exponential factor, ω is the angular frequency, and n is the frequency exponent ($0 \leq n \leq 1$) related to the dynamic of hopping ions [44]. The change of n with temperature is given as inset in Fig. 8. The exponent "*n*" displays a virtually linear growth with temperature until the transition zone (50–60 °C), and subsequently, reorganization of nanocomposite takes place at a specified temperature interval. Over the transition zone, it kept on increasing with a remarkable increment in slope at higher temperatures which is a good agreement with conductivity. This behavior can be interpreted as interactions between mobile ions increases, the value of n regularly increases, i.e., the process is wholly frequency independent when $n = 0$. The n values vary between 0.02 and 0.77 in the present study. The variation of n values with temperature suggests that the conduction phenomena is a thermally activated polarization process. The low n values are probably due to the strong electrode polarization.

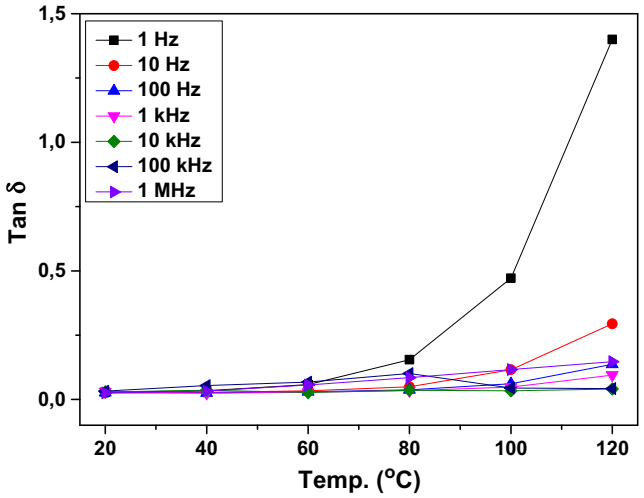

Fig. 8 The variation of tan δ (dissipation factor) for OAm functionalized $NiFe_2O_4$ NPs as a function of frequency and temperature

The variation of the loss tangent (tan δ) of OAm functionalized $NiFe_2O_4$ NPs with temperature at different frequencies is displayed in Fig. 8. The tan δ, in general, decreases with increasing frequency while keeping the temperature constant. The conductivity of OAm functionalized $NiFe_2O_4$ NPs is rather small in low frequencies due to grain boundary which gives rise to a higher energy requirement for electron transfer between Fe^{2+} and Fe^{3+} ions. In a high-frequency region, on the contrary, small energy is necessary for the transfer of electrons as the conductivity of nanoparticles is comparatively high because of grains. The loss tangent grows slightly with an increase in temperature whereas influence of temperature is maximum at 1 Hz. The polarization mechanism is used to describe the temperature dependency of loss tangent. With increasing temperature, mobility of the charge carrier increases which in return cause an enhancement in electrical conductivity. Subsequently, the dielectric constant and dielectric loss tangent enhance since the dielectric polarization increases at lower temperatures.

4 Conclusion

From all the above studies, nearly monodispersed nanoparticles of $NiFe_2O_4$ have been prepared with very high size selectivity under a thermal decomposition condition. In addition, we discovered that only oleylamine as a reducing agent, surfactant, and stabilizing agent could be used as "multifunctional role." Also, the long chain alcohol is essential for the nucleation and growth process since it probably helps ferric cations available to particularly enhance the synthesis of ferrites. The synthesis method makes them possible to be a general approach for the preparation of other pure binary and ternary compounds. The ac conductivity exhibited two different behaviors: a frequency dependency in the low-frequency region and a temperature independency in the high-frequency region. These variation is a clear suggestion for ionic conductivity which is principally based on the hopping process. With increasing temperature, a more organized structure is formed so that nanoparticles show more capacitive behavior and fairly low-frequency response leading to an increase in the increment in conductivity. The dc conductivity increases linearly with temperature including the transition zone (50–60 °C) and maximum conductivity of 4. 37 $\times$ 10^{-12} S.cm^{-1} at 120 C. The variation of frequency exponent n values with temperature is described by thermally activated polarization mechanism. The activation energies (E_a) for the two distinct regions were calculated as 0.0351 and 0.299 eV which may explain to have such low conductivities for this OAm functionalized $NiFe_2O_4$ NPs. The dielectric constants (ε' and ε'') indicate remarkable frequency and temperature dependency. The reduction in dielectric constants with increasing frequency is perhaps due to the increase of electron exchange between Fe^{2+} and Fe^{3+} ions. The dielectric measurements confirm that the conduction is governed by both temperature and the diversity of the reorganization of NPs. As a result, the observed conductivity and dielectric properties of OAm functionalized $NiFe_2O_4$ NPs may suggest various promising applications such as drug carrier and bioseparator, chemical sensors and biosensors, and metal ion separation from waste water.

Acknowledgments This work is supported by Fatih University under BAP grant no P50031504_B.

References

1. Khairy, M., Gouda, M.E.: J. Adv. Res. **6**, 555–562 (2015)
2. Sözeri, H., Deligöz, H., Kavas, H., Baykal, A.: Ceram. Int. **40**, 8645–8657 (2014)
3. Gul, I.H., Maqsood, A.: J. Alloys Compd. **465**, 227–231 (2008)
4. Khafagy, R.M.: J. Alloys Compd. **509**, 9849–9857 (2011)
5. Khairy, M.: Synth. Met. **189**, 34–41 (2014)
6. Shi, Z., Zhang, J., Gao, D., Zhu, Z., Yang, Z., Zhang, Z., Xue, D.: Nanoscale Res. Lett. **8**, 1–5 (2013)
7. Martins, P., Costa, C.M., Lanceros-Mendez, S.: Appl. Phys. A **103**, 233–237 (2010)
8. Sabale, S., Jadhav, V., Khot, V., Zhu, X., Xin, M., Chen, H.: J. Mater. Sci. Mater. Med. **26**, 1–9 (2015)
9. Luo, L., Cui, R., Liu, K., Qiao, H., Wei, Q.: Ionics **21**, 687–694 (2014)

10. Umare, S.S., Ningthoujam, R.S., Sharma, S.J., Shrivastava, S., Kurian, S., Gajbhiye, N.S.: Hyperfine Interact. **184**, 235–243 (2008)
11. Kooti, M., Sedeh, A.N.: J. Mater. Sci. Technol. **29**, 34–38 (2013)
12. Naseri, M.G., Saion, E.B., Ahangar, H.A., Hashim, M., Shaari, A.H.: Powder Technol. **212**, 80–88 (2011)
13. Sertkol, M., Köseoğlu, Y., Baykal, A., Kavas, H., Bozkurt, A., Toprak, M.S.: J. Alloys Compd. **486**, 325–329 (2009)
14. Sözeri, H., Alveroğlu, E., Kurtan, U., Şenel, M., Baykal, A.: J. Supercond. Nov. Magn. **26**, 213–218 (2012)
15. Xu, Z., Shen, C., Hou, Y., Gao, H., Sun, S.: Chem. Mater. **21**, 1778–1780 (2009)
16. Sun, S., Zeng, H.: J. Am. Chem. Soc. **124**, 8204–8205 (2002)
17. Kurtan, U., Güngüneş, H., Sözeri, H., Baykal, A.: Ceram. Int. doi:10.1016/j.ceramint.2016.01.200
18. Zi, Z., Sun, Y., Zhu, X., Yang, Z., Dai, J., Song, W.: J. Magn. Magn. Mater. **321**, 1251–1255 (2009)
19. Baruwati, B., Manorama, S.V.: Mater. Chem. Phys. **112**, 631–636 (2008)
20. Mourdikoudis, S., Liz-Marzán, L.M.: Chem. Mater. **25**, 1465–1476 (2013)
21. Karaoğlu, E., Özel, U., Caner, C., Baykal, A., Summak, M., Sözeri, H.: Mater. Res. Bull. **47**, 4316–4321 (2012)
22. Li, X.-H., Xu, C.-L., Han, X.-H., Qiao, L., Wang, T., Li, F.-S.: Nanoscale Res. Lett. **5**, 1039–1044 (2010)
23. Ünal, B., Durmus, Z., Baykal, A., Sözeri, H., Toprak, M.S., Alpsoy, L.: J. Alloys Compd. **505**, 172–178 (2010)
24. Baykal, A., Bıtrak, N., Ünal, B., Kavas, H., Durmus, Z., Özden, Ş., Toprak, M.S.: J. Alloys Compd. **502**, 199–205 (2010)
25. Unal, B., Durmus, Z., Kavas, H., Baykal, A., Toprak, M.: Mater. Chem. Phys. **123**, 184–190 (2010)
26. Baykal, A., Erdemi, H., Amir, M.: J. Inorg. Organomet. Polym. Mater. **26**, 190–196 (2016)
27. Erdemi, H., Baykal, A., Karaoğlu, E., Toprak, M.S.: Mater. Res. Bull. **47**, 2193–2199 (2012)
28. Günay, M., Erdemi, H., Baykal, A., Sözeri, H., Toprak, M.S.: Mater. Res. Bull. **48**, 1057–1064 (2013)
29. Shirsath, S.E., Toksha, B.G., Mane, M.L., Dhage, V.N., Shengule, D.R., Jadhav, K.M.: Powder Technol. **212**, 218–223 (2011)
30. Lupeiko, T., Lopatina, I., Kozyrev, I., Derbaremdiker, L.: Inorg. Mater. **28**, 481–485 (1992)
31. Verwey, E., De Boer, F., Van Santen, J.: J. Chem. Phys. **16**, 1091–1092 (1948)
32. Rao, B.P., Rao, K., Sankaranarayana, G., Paduraru, A., Caltun, O.: J. Optoelectron. Adv. Mater. **7**, 697–700 (2005)
33. Pardavi-Horvath, M.: J. Magn. Magn. Mater. **215**, 171–183 (2000)
34. Iqbal, M.J., Ismail, B.: J. Alloys Compd. **504**, 440–445 (2010)
35. Deligöz, H., Özgümüş, S., Yalçınyuva, T., Yıldırım, S., Deger, D., Ulutaş, K.: Polymer **46**, 3720–3729 (2005)
36. Sözeri, H., Mehmedi, Z., Erdemi, H., Baykal, A., Topal, U., Aktaş, B.: Ceram. Int. **42**, 2611–2625 (2016)
37. Erdemi, H., Demir, A., Baykal, A.: J. Inorg. Organomet. Polym. Mater. **23**, 690–702 (2013)
38. Okada, T., Satou, H., Okuno, M., Yuasa, M.: J. Phys. Chem. B **106**, 1267–1273 (2002)
39. Mahalakshmi, S., Manja, K.S.: J. Alloys Compd. **457**, 522–525 (2008)
40. Verwey, E., De Boer, J.: Recueil des Travaux Chimiques des Pays-Bas **55**, 531–540 (1936)
41. David, R.C., Griffiths, J. Introductionto Electrodynamics, 3rd ed. Prentice Hall (1998)
42. Jackson, J.D. Classical Electrodynamics, 3rd ed. Wiley, New York (1998)
43. Stergiou, C.A., Manolakis, I., Yioultsis, T.V., Litsardakis, G.: J. Magn. Magn. Mater. **322**, 1532–1535 (2010)
44. Habasaki, J., Ngai, K.: J. Non-Cryst. Solids **352**, 5170–5177 (2006)